reduced in the Norwegian Sea it may increase in the Labrador Sea, so that the two regions act like a see-saw. Climate cooling is then not caused by an overall weakening of the conveyor, but by a reduction in its heat transport related to the higher temperature of Labrador Sea convection.

These model experiments demonstrate that in order to explain rapid cooling events we need not invoke a total collapse of the conveyor; rather more subtle changes can cause a temperature drop in the northern North Atlantic of up to 5 °C. □

Received 16 June; accepted 23 September 1994.

1. Veum, T. *et al. Nature* **356,** 783–785 (1992).
2. Lehman, S. J. & Keigwin, L. D. *Nature* **356,** 757–762 (1992).
3. Zahn, R. *Nature* **356,** 744–746 (1992).
4. Boyle, E. A. & Keigwin, L. *Nature* **330,** 35–40 (1987).
5. Keigwin, L. D. *et al. J. geophys. Res.* **96,** 16811–16826 (1991).
6. Trenberth, K. E. & Solomon, A. *Clim. Dyn.* **10,** 107–134 (1994).
7. Levitus, S. *Climatological Atlas of the World Ocean* (US Dept of Commerce, NOAA, Washington DC, 1982).
8. Manabe, S. & Stouffer, R. J. *J. Clim.* **1,** 841–866 (1988).
9. Maier-Reimer, W. & Mikolajewicz, U. in *Oceanography* (eds Ayala-Castañares, A., Wooster, W. & Yáñez-Arancibia, A.) 87–100 (UNAM, México, 1989).
10. Marotzke, J. & Willebrand, J. *J. phys. Oceanogr.* **21,** 1372–1385 (1991).
11. Haney, R. L. *J. phys. Oceanogr.* **1,** 241–248 (1971).
12. Rahmstorf, S. & Willebrand, J. *J. phys. Oceanogr.* (in the press).
13. Sarnthein, M. *et al. Paleoceanography* **9,** 209–267 (1994).
14. Kushnir, Y. *J. Clim.* **7,** 142–157 (1994).
15. Rahmstorf, S. *J. Clim.* (in the press).
16. Stommel, H. *Tellus* **13,** 224–230 (1961).
17. Welander, P. *Dyn. Atmos. Oceans* **6,** 233–242 (1982).
18. Lenderink, G. & Haarsma, R. J. *J. phys. Oceanogr.* **24,** 1480–1493 (1994).
19. Fairbanks, R. G. *Nature* **342,** 637–642 (1989).
20. Weaver, A. J. & Hughes, T. M. C. *Nature* **367,** 447–450 (1994).
21. Send, U. & Marshall, J. *J. phys. Oceanogr.* (in the press).
22. Lehman, S. J. & Keigwin, L. D. *Nature* **358,** 197–198 (1992).

ACKNOWLEDGEMENTS. I thank J. Willebrand for assistance, R. Zahn, M. Rhein and E. Suess for discussions, and D. Smart for improving the clarity of the language in this Letter. This work was supported by the Deutsche Forschungsgemeinschaft; computations were performed at the German Climate Computer Centre in Hamburg.

Experimental simulations of explosive degassing of magma

H. M. Mader*, Y. Zhang†, J. C. Phillips‡, R. S. J. Sparks‡, B. Sturtevant§ & E. Stolper‖

* Institute of Environmental and Biological Sciences, Lancaster University, Lancaster LA1 4YQ, UK
† Department of Geological Sciences, University of Michigan, Ann Arbor, Michigan 48109–1063, USA
‡ Department of Geology, University of Bristol, Bristol BS8 1RJ, UK
§ Graduate Aeronautical Laboratories, ‖ Division of Geological and Planetary Sciences, California Institute of Technology, Pasadena, California 91125, USA

THE violent release of volatiles in explosive volcanic eruptions is known to cause fragmentation of magma and acceleration of the resulting mixture of gas and pyroclasts to velocities exceeding 100 m s^{-1} (ref. 1). But the mechanisms underlying bubble nucleation, flow acceleration and fragmentation are complex and poorly understood. To gain insight into these phenomena, we have simulated explosive eruptions using two model systems that generate expansion rates and flow velocities comparable to those observed in erupting volcanos. The key feature of both experiments is the generation of large supersaturations of carbon dioxide in a liquid phase, achieved either by decompressing CO_2-saturated water or by rapid mixing of concentrated K_2CO_3 and HCl solutions. We show that liberation of CO_2 from the aqueous phase is enhanced by violent acceleration of the mixture, which induces strong extensional strain in the developing foam. Fragmentation then occurs when the bubble density and expansion rate are such that the bubble walls rupture. In contrast to conventional models of fragmentation[1,2], we find that expansion and acceleration precede—and indeed cause—fragmentation.

The experiments were carried out (Fig. 1) at the University of Bristol and the California Institute of Technology using shock-tube techniques first proposed in this context by Bennett[3] and more recently developed in studies of volcanic jets[4], explosive vaporization[5] and high-speed dense dusty gases[6,7]. A crucial characteristic of the natural systems that we have tried to match in our experiments is that the volatile component (largely H_2O and/or CO_2 in real volcanic eruptions) is in a gaseous state after exsolution but the liquid component (in nature, a silicate liquid ± crystals), which makes up most of the mass of the system, is essentially entirely condensed, even after the volatile component has nearly completely exsolved. In these respects the systems in our experiments differ significantly from one-component systems[5] and two-component systems that completely (or nearly completely) evaporate on decompression.

Design of small-scale experiments to model large-scale volcanic phenomena requires consideration of scaling and dynamic similarity, but no scaling relationships have been established[8] for rapidly degassing bubbly liquids or the high-velocity high-density gas–particle flows that they generate[7]. Thus it is desirable to conduct simulations at the same velocity and with accelerations and flow densities similar to those in the large-scale setting. Velocities in our experiments approach those of volcanic flows (~100 m s^{-1})[1], as do the accelerations (~100g, ref. 7; note that gravity (1g) is unimportant in flows that experience such large accelerations). The high velocities and accelerations experienced by these flows mean that inertial rather than viscous forces control the dynamics. The ratio of the test-cell pressure to reservoir pressure in the decompression experiments (Fig. 1*a*) ranges from 30 to 300, comparable to magmas with a few per cent dissolved water (saturation pressures ~50–100 MPa) that disrupt explosively at a few megapascals (refs 2, 9). Obviously, the length scales of the volcanic system cannot be reproduced in the laboratory. Generally, in the study of bubbly liquids and dusty gases, the diameter of the laboratory flow channel is chosen to be much larger than the smallest bubble or particle class being modelled[7,10] so that the long-range dynamical interactions between phases that generate a variety of flow scales are free to act.

Bubble nucleation and growth are ultimately the processes that drive the accelerations observed in our experiments, so scaling of our results to nature requires an evaluation of how they may differ in supersaturated magmas. Molar fractions of volatiles in our experiments (up to 0.004 for CO_2 in the depressurization experiments, and as large as 0.1 in the chemical injection experiments) are comparable to those of intermediate to silicic magmas (0.02–0.06 for H_2O)[2], so the ratio of gas to condensed matter is comparable in the experiments and in nature. However, the diffusivity of CO_2 in H_2O (2×10^{-9} m^2 s^{-1} at 20 °C)[11] is ~200 times larger than that of H_2O (at concentrations of about 0.03) in magma at 850 °C (~10^{-11} m^2 s^{-1})[12,13]. The diffusively-controlled volume growth rate of bubbles during degassing is proportional to the product of diffusivity and concentration, which ranges from ~10 times larger than in magma in the decompression experiments to locally 200 times in the chemical experiments. The viscosity of water is also many orders of magnitude less than that of magma in explosive eruptions. But numerical calculations (ref. 14 and J. Barclay, D. S. Riley and R.S.J.S., unpublished results) indicate that, even under conditions of explosive eruption, diffusive bubble growth is not retarded by viscous effects unless magma viscosities exceed 10^8 Pa s. In the fragmentation region, with pressures of a few megapascals, magmas are not fully degassed and a few tenths of a per cent of residual dissolved water are sufficient to keep viscosities at values that would not inhibit explosive expansion

rates[2]. Initial bubble densities measured in the decompression experiments are of the order of 10^9 m^{-3}, whereas in laboratory experiments on volcanic glasses[15] densities of the order of 2×10^{14} m^{-3} have been reported; observations of pumice[16,17] suggest nucleation densities of 3×10^{14} to 3×10^{16} m^{-3}. That bubble densities in the present experiments are up to 5 orders of magnitude smaller than in nature and in decompression experiments on magmatic compositions is probably more important than the smaller difference in diffusivities noted above and suggests that natural events could be even more explosive than those observed by us in the laboratory.

Figure 2 shows representative single frames taken from high-speed motion pictures of the two experiments. In the experiment of Fig. 2*a*, velocities up to 14 m s^{-1} and accelerations of more than 200*g* are observed for supersaturation pressures of 0.7 MPa. The flows expand at almost constant acceleration (Fig. 3*a*), which is strongly and positively correlated with the ratio of test-cell pressure to reservoir pressure, and weakly negatively correlated with liquid viscosity. As bubble growth causes expansion and the number of bubbles remains constant following initial nucleation (suggesting heterogeneous nucleation), constant acceleration implies that the bubble volume increases in proportion to t^2 (where t is time), or the bubble diameter increases as $t^{2/3}$. Preliminary measurements on individual bubbles, during the time when bubbles are well-separated and roughly spherical, confirm this relationship. In the flows generated by chemical reaction (Fig. 2*b*), peak velocities and accelerations increase with CO_2 supersaturation (Fig. 3*b*). CO_2 supersaturations up to 9 MPa, velocities up to 30 m s^{-1} and accelerations up to 150*g* are achieved when saturated K_2CO_3 (6 M) is injected into concentrated HCl (12 M). The acceleration of these flows increases approximately linearly with time because

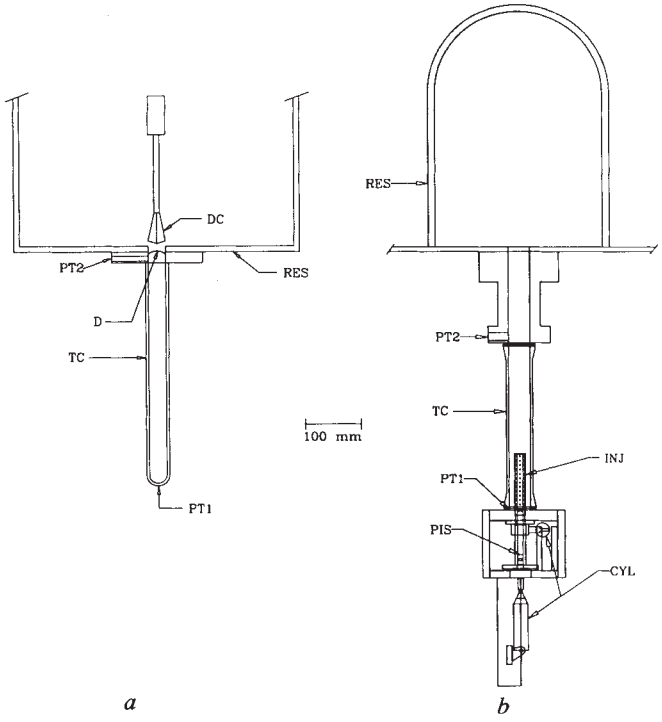

FIG. 1 Schematic diagram of the experimental apparatus. Water saturated with CO_2 is generated in the test cell TC made of Pyrex pipe and erupts into the reservoir RES. Pressures are measured with fast-response piezoelectric transducers at the bottom of the test cell PT1 and at the exit PT2. The flows are visualized by high-speed motion-picture photography at rates up to 6,000 frames per second. *a*, Apparatus at Caltech[5]. The test cell is partially filled with CO_2–saturated H_2O at pressures up to 0.7 MPa. The reservoir is evacuated to ~7 kPa. Sudden decompression and supersaturation is achieved by puncturing a diaphragm D with a solenoid-driven diaphragm cutter DC. Gas is released from the liquid progressively by bubble nucleation, growth and foam formation. Bubble growth and foam expansion are limited by mass diffusion of solute to the bubble walls. The viscosity of the test mixture was varied from that of water (10^{-3} Pa s) to 0.7 Pa s by the addition of up to 1% organic polymer. *b*, Apparatus at Bristol University. A quantity (4 ml) of K_2CO_3 solution is injected in a few milliseconds through 96 holes in injector INJ into the test cell, which initially contains a much larger volume (100 cm^3) of HCl solution (up to the top of INJ). Mixing of the reactants initially occurs on the boundaries of the 96 jets and later due to stretching of fluid elements as the gas–liquid mixture accelerates up the test cell. The rate of the ensuing chemical reaction is limited by fluid-mechanical mixing and the rate-limiting step $H_2CO_3 \leftrightarrow CO_2 + H_2O$, with reaction timescale (the time for the reactant to reach 1/e of its initial concentration) about 70 ms. Production of vapour-phase CO_2 is further limited by mass diffusion. By using high concentrations of the reactants, very large gas yields are achieved with theoretical supersaturation pressures up to several megapascals. The pneumatic cylinders CYL, which drive piston PIS to inject the K_2CO_3 and open the 96 holes, are computer-controlled.

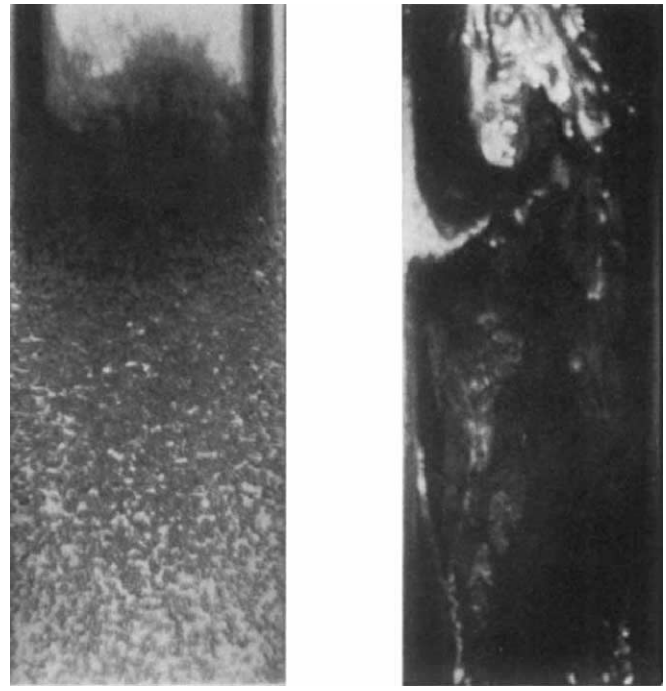

FIG. 2 Photographs of the early development of simulated eruptions. The views are back lit. Light areas are bubble-free liquid or drop-free vapour. A large density of bubbles or droplets scatters light from the beam making the medium opaque (dark). *a*, Flow generated by depressurization. Image of the test cell from 4 to 13 cm above its base. Initial cell pressure, 565 kPa; initial tank pressure, 6.9 kPa. The photograph shows the test solution, initially 10 cm deep, 7.1 ms after depressurization. Bubbles nucleate uniformly (~10^3 cm^{-3}) throughout the solution immediately on depressurization, and negligible nucleation occurs thereafter. Bubbles near the top of the mixture grow faster than those below. The flow in the photograph has expanded to 12 cm height. Above 10.5 cm the liquid is finely fragmented, while between 9.5 and 10.5 cm the bubbles have merged into a rapidly accelerating foam. The bubbles in the foamed region are stretched in the flow direction. Fragmentation appears to occur by the bursting of bubbles on a very irregular surface, due perhaps to a combination of over-pressurization, rapid stretching and violent interaction with neighbouring bubbles. *b*, Flow generated by chemical reaction. Image of the test cell from 29 cm to 38 cm above its base. The photograph shows the test solution, initially 9.7 cm deep, 34 ms after the initiation of the chemical reaction. Bubble nucleation begins after an incubation time of the order of 5 ms and continues over the timescale of the experiment, as the expanding flow produces strong mixing of the reactants. The resulting foam is highly heterogeneous, with fragmentation occurring in the regions of most violent gas release.

of continuous mixing of the reactants, which is itself enhanced by the stretching of the accelerating two-phase mixture. Eventually the acceleration reaches a maximum and then decreases when the reactants are depleted.

The two sets of experiments reveal several aspects of the physics of violent degassing.

(1) The growth rate measured in the decompression experiments is greater than the $t^{1/2}$ power-law behaviour expected for diffusive growth of a spherical bubble at rest in an infinite fluid and frequently used in models of explosive volcanic eruptions[2,18].

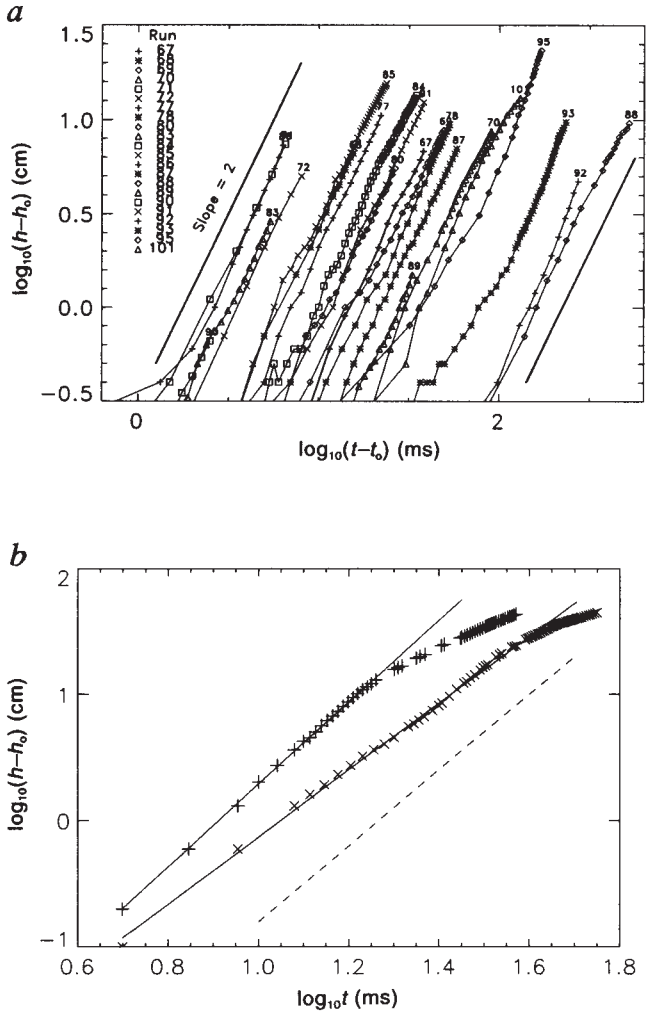

FIG. 3 Position of the flow head h as a function of time t measured from high-speed motion pictures. *a*, Flow generated by depressurization. Log–log (base 10) plot of $h-h_0$ against t. Origin of time, $0 \leqslant t_0 \leqslant 22.5$ ms, was adjusted for each run to optimize the linearity of the plot. Results of 22 runs at different saturation pressure, ambient pressure, fluid viscosity and fill depth are shown. Lines of slope 2 (constant acceleration) are indicated at right and left. The acceleration increases monotonically from right to left on the plot from 0.7 m s^{-2} (run 88) to 2,100 m s^{-2} (run 90). *b*, Flow generated by chemical reaction. Top curve, 6 M K_2CO_3→12 M HCl; bottom curve, 6 M K_2CO_3→6 M HCl. Each curve is a composite of data from five films viewing different parts of the test cell. The origin of time for each film was selected to ensure continuity of the plotted data. A least-squares fit (solid lines) of the initial linear part of the data was made to the function $h-h_0=At^b$ where h_0 is the initial height of the liquid in the test cell, with the following results: 6 M K_2CO_3→6 M HCl, $b=2.69$, $A=1.49\times10^{-3}$; 6 M K_2CO_3→12 M HCl, $b=3.26$, $A=1.07\times10^{-3}$. As $b>2$, these flows experience accelerations that increase with time and with CO_2 yield. Line of slope 3 ($a \propto t$) is shown on the right (dashed).

The observed $t^{2/3}$ growth rate has, however, been predicted theoretically[19] for bubbles moving with constant convective velocity U relative to supersaturated liquid. One mechanism for inducing convective motion of bubbles in these experiments and in erupting magmas is buoyant rise in the rapidly-accelerating fluid. Constant-velocity (that is, independent of bubble diameter) buoyant rise occurs in a regime of bubble motion dominated by capillarity and gravity, when $We^3/Fr>100$ (ref. 20), where $We=\rho U^2 D/\sigma$ is the Weber number, $Fr=U^2/aD$ is the Froude number, ρ is the liquid density, D is the bubble diameter, σ is the surface tension and a is the acceleration. Under these conditions $U=1.2(\sigma a/\rho)^{1/4}$. Thus the rise velocity depends weakly on acceleration and surface tension and, for the experiments reported here ($a=100g$, $\sigma=0.07$ N m^{-1}, $\rho=1{,}000$ kg m^{-3}) is ~0.6 m s^{-1}; $We^3/Fr=6{,}000$ for $D=2\times10^{-3}$ m. Although bubble rise under different laboratory conditions or in magmatic systems will probably be in a different regime of bubble rise, our experiments demonstrate that in general degassing in explosively accelerating liquids is enhanced by buoyant convective diffusion.

(2) In the chemically-generated flows, large gradients of HCl concentration near the injection jets generate large supersaturation gradients and spatially inhomogeneous liberation of CO_2 vapour. Therefore, the chemically-generated two-phase flows are intrinsically heterogeneous, and thus they may model the behaviour of inhomogeneities occurring in real natural systems. This difference between the two types of flows is visible in Fig. 2; striations of differing opacity, varying from clear (no bubbles) to black (highly vesiculated, fragmented) appear throughout the image of Fig. 2*b*, whereas the dark, high-bubble-density fragmentation region in Fig. 2*a* is confined to the neighbourhood of the free surface. In the chemically-generated flow, even liquid below virtually bubble-free clear fluid (Fig. 2*b*, top) is fragmented. Evidence of heterogeneous vesiculation is common in plinian pyroclastic deposits and ignimbrites.

(3) In our experiments, water fragments into a spray entirely in the liquid state, demonstrating that fragmentation induced by rapid expansion in the liquid state can occur as well in volcanic systems. But in contrast to water, silicic magmas exhibit viscoelastic behaviour[21] at strain rates comparable to those observed in our experiments; we observe accelerations to 50 m s^{-1} in distances of less than 1 m, so the extensional strain rate is of the order of 100 s^{-1}. In the Maxwell model of linear viscoelastic materials, the relaxation time τ is given approximately by $\tau=\mu/G$, where μ is the shear viscosity and G is the shear modulus[22]. With $\mu\approx10^8$ Pa s for magma with a few weight per cent H_2O at eruption temperature[2] and $G\approx10^{10}$ Pa, then $\tau\approx10^{-2}$ s, of the same order as the inverse strain rate in rapid exsolution. Thus rapid expansion sufficient to cause magma to cross the glass transition, leading to brittle fracture of the foam, may be possible. Future experiments will examine this mechanism in model viscoelastic fluids.

(4) An important result of our experiments is that models[1,2] postulating that magma fragments at a simple downward-propagating front in almost static foams with vesicularities of 0.7–0.8, and that flow expansion occurs after fragmentation, should be revised. Foam acceleration precedes fragmentation, rather than the reverse. In addition, in some of the depressurization experiments, vesicularities in excess of 0.7–0.8 are achieved without fragmentation. Silicic pumices with high vesicularities are also known[23].

Convectively-enhanced degassing and the mechanisms of flow expansion and fragmentation will, when incorporated into theoretical models of eruption dynamics, significantly affect such parameters as flow velocity and density at the conduit exit, and the duration of eruptions. Consequently, new insight gained from these experimental simulations could have an important impact on the theoretical prediction of volcanic phenomena and hazards. □

Received 28 March; accepted 28 September 1994.

1. Wilson, L., Sparks, R. S. J. & Walker, G. P. L. *Geophys. J. R. astr. Soc.* **63,** 117–148 (1980).
2. Sparks, R. S. J. *J. Volcan. geotherm. Res.* **3,** 1–37 (1978).
3. Bennett, F. D. *Nature* **234,** 538–539 (1971).
4. Kieffer, S. W. & Sturtevant, B. *J. geophys. Res.* **89,** 8253–8268 (1984).
5. Hill, L. G. & Sturtevant, B. in *Adiabatic Waves in Liquid–Vapor Systems* (eds Meier, G. E. A. & Thompson, P. A.) 25–37 (Springer, Berlin, 1990).
6. Anilkumar, A. V. thesis, California Inst. Technol. (1989).
7. Anilkumar, A. V., Sparks, R. S. J. & Sturtevant, B. *J. Volcan. geotherm. Res.* **56,** 145–160 (1993).
8. Barnea, D. & Taitel, Y. in *Encyclopedia of Fluid Mechanics* (ed. Cheremisinoff, N. P.) Ch. 16 (Gulf, Houston, 1985).
9. Wilson, L. *J. Volcan. geotherm. Res.* **8,** 297–313 (1980).
10. Sangani, A. S. in *Encyclopedia of Fluid Mechanics* (ed. Cheremisinoff, N. P.) Ch. 5 (Gulf, Houston, 1985).
11. Cussler, E. L. *Diffusion: Mass Transfer in Fluid Systems* (Cambridge Univ. Press, 1984).
12. Zhang, Y., Stolper, E. M. & Wasserburg, G. J. *Geochim. cosmochim. Acta,* **1,** 1–16 (1990).
13. Zhang, Y., Stolper, E. M. & Wasserburg, G. J. *Earth planet. Sci. Lett.* **103,** 228–240 (1990).
14. Dobran, F. *J. Volcan. geotherm Res.* **49,** 285–311 (1992).
15. Navon, O. & Hurwitz, S. *Terra abstr.* **5,** 574 (1993).
16. Sparks, R. S. J. & Brazier, S. *Nature* **295,** 218–220 (1982).
17. Whitham, A. G. & Sparks, R. S. J. *Bull. volcan.* **48,** 209–223 (1986).
18. Toramaru, A. *J. geophys Res.* **94,** 17523–17542 (1989).
19. van Wijngaarden, L. *Int. J. Heat Mass Transfer* **10,** 127–134 (1967).
20. Peebles, F. N. & Garber, H. J. *Chem. Engng. Prog.* **49,** 88–97 (1953).
21. Dingwell, D. B. & Webb, S. L. *Phys. Chem. Miner.* **16,** 508–516 (1989).
22. Scherer, G. W. *Relaxation in Glass and Composites* (Wiley, New York, 1986).
23. Klug, C. & Cashman, K. V. (abstr.) *EOS* **72,** 312 (1991).

ACKNOWLEDGEMENTS. This work was supported by the UK National Environmental Research Council, the BP Venture Fund, the US NSF, the California Institute of Technology and the University of Michigan.

Optimal harvesting, economic discounting and extinction risk in fluctuating populations

Russell Lande*, Steinar Engen† & Bernt-Erik Saether‡

* Department of Biology, University of Oregon, Eugene, Oregon 97403-1210, USA
† Department of Mathematics and Statistics, University of Trondheim AVH, N-7055 Dragvoll, Norway
‡ Norwegian Institute for Nature Research, Tungasletta 2, N-7004 Trondheim, Norway

DETERMINISTIC models demonstrate that when the economic discount rate of future harvests exceeds a critical value related to population growth rate, the strategy that maximizes the present value of cumulative harvest is immediate extinction (liquidation) of the population[1–3]. Here we analyse stochastic models to derive optimal strategies that maximize the expected present value of cumulative harvest before extinction of a fluctuating population. Stochastic models reveal that discount rates below the critical value can substantially reduce the mean time to extinction and the expected real harvest before extinction. With an unstable equilibrium at small population size (Allee effect[4–6] or depensation[2]), the critical discount rate is lower in the stochastic model than in the corresponding deterministic model. These results argue against economic discounting in the development of optimal strategies for sustainable use of biological resources.

Commercially important species are often overharvested to economic depletion (many fisheries and forest-dwelling species[7,8]), to near extinction (the blue whale, right whale, northern elephant seal, American bison, black rhino, white rhino, for example[9–13]), or to extinction (Stellar's sea cow, great auk, Caribbean monk seal[10,14]). Overexploitation, usually combined with habitat destruction and/or introduced species, threatens about one-third of the endangered mammals and birds of the world[10].

Optimal harvesting policies that maximize profit may fail to achieve sustainable use of renewable resources. Economists note that entrepreneurs typically discount future income at a rate equal to or greater than the real interest rate (monetary interest rate minus inflation rate)[1,2]. When the discount rate, δ, exceeds a critical value, δ^*, deterministic models of population growth show that the economically optimal strategy is immediate harvesting to extinction[1–3] (Fig. 1). When the discount rate is below the critical value, deterministic models predict a perpetual constant harvest.

Real populations fluctuate because of demographic and environmental stochasticity (individual and temporal variation) in birth and death rates, and palaeontology indicates that extinction is the eventual fate of all species[15,16]. Stochastic models demonstrate that population fluctuations reduce the maximum expected harvest below the deterministic maximum sustained yield (MSY)[17–19]; this and the collapse of many fisheries discredited the MSY concept[7]. However, economic discounting and the dynamics of extinction have received little attention in stochastic harvesting models.

Denote the mean annual change in a population of size N as $M(N) = M_0(N) - y(N)$, where $M_0(N)$ represents the expected dynamics without harvesting and $-y(N)$ is the reduction from harvesting. The variance of annual change in population, given the present size, is $V(N)$. The discount rate and the profit per unit harvest are assumed to be constants. If N_t is the population size at time t, then from an initial population N_0 the expected present value of cumulative harvest before extinction is

$$\psi(N_0, \delta) = E\left[\int_0^{t^*} e^{-\delta t} y(N_t)\, dt\right] \quad (1)$$

where t^* is the extinction time of a particular population in a stochastic environment. Assuming that proportional changes in population per year are usually small, as for large-bodied birds

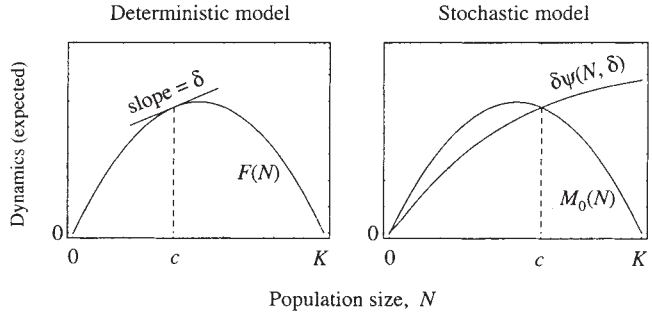

FIG. 1 Optimal harvesting strategies in deterministic and stochastic population models, assuming a constant profit per unit harvest. In the deterministic model, the population dynamics in the absence of harvesting are $dN/dt = F(N)$. The population size that maximizes the present value of future harvests, c, occurs where the slope of the population growth curve equals the discount rate[1,2], $F'(c) = \delta$. There may be zero, one or more solutions; the optimal strategy is the solution with the largest sustained yield. When the discount rate exceeds a critical value, δ^*, equal to the maximum $F'(N)$ with $F(N) > 0$, there is no solution and the optimal strategy is immediate harvesting to extinction. The stochastic model has expected dynamics $M_0(N)$ without harvesting. The optimal harvesting threshold, c, above which all excess individuals are immediately harvested and below which no harvesting occurs, maximizes the expected present value of cumulative yield before extinction, ψ, defined in equation (1). c is approximately a solution of $M_0(c) = \delta\psi(c, \delta)$. There may be zero, one, or more solutions. The optimal strategy corresponds either to the solution producing the largest ψ or to $c = 0$. If there is no solution, or if $c = 0$ gives a larger ψ, then the optimal strategy is immediate harvesting to extinction. The (expected) population dynamics illustrated for both the deterministic and stochastic models are given in Fig. 2, and the values of c shown are for $\delta = 0.01$ per year.